

Navier-Stokes Computations of Longitudinal Forces and Moments for a Blended Wing Body

S. Paul Pao*, Robert T. Biedron[†], Michael A. Park[‡], C. Michael Fremaux[§], and
Dan D. Vicroy[¶]

NASA Langley Research Center, Hampton, VA 23681

Abstract

The object of this paper is to investigate the feasibility of applying CFD methods to aerodynamic analyses for aircraft stability and control. The integrated aerodynamic parameters used in stability and control, however, are not necessarily those extensively validated in the state of the art CFD technology. Hence, an exploratory study of such applications and the comparison of the solutions to available experimental data will help to assess the validity of the current computation methods. In addition, this study will also examine issues related to wind tunnel measurements such as measurement uncertainty and support interference effects. Several sets of experimental data from the NASA Langley 14x22-Foot Subsonic Tunnel and the National Transonic Facility are presented. Two Navier-Stokes flow solvers, one using structured meshes and the other unstructured meshes, were used to compute longitudinal static stability derivatives for an advanced Blended Wing Body configuration over a wide range of angles of attack. The computations were performed for two different Reynolds numbers and the resulting forces and moments are compared with the above mentioned wind tunnel data.

Introduction

Wind tunnel testing is becoming increasingly expensive, and the number of facilities available for testing is decreasing. At the same time, the cost of computing has dropped dramatically. There is a growing awareness that Computational Fluid Dynamics (CFD) will need to be validated for the task of reliably analyze the static and dynamic stability characteristics of future aircraft systems. However, many of the innovative vehicle concepts being considered have unconventional vehicle geometry. The placement of control surfaces and the interactions between them may be very different from that of traditional designs. The drive towards ultra high efficiency commercial transport systems requires precise knowledge of all aspects of aerodynamics, propulsion, stability and control (S&C), and component flow physics, including nonlinear effects.

This expanding requirement to use CFD for S&C brings formidable challenges to the CFD community. Current applications of CFD are generally focused upon the mission performance aspects of the airplane such as lift and drag for the cruise segment of the flight, and high lift devices for the terminal operation segments. In these operational segments, true also at high lift conditions, attached flow is often the norm, with the exception that mildly separated flow or shed vortex dynamics may be important in some cases. Even still lift and drag coefficients are a challenge, other flight conditions, such as side slip, would normally be studied with much less emphasis. As a consequence, most of the current CFD validation analysis has to do with lift and drag coefficients.

For a typical six degree-of-freedom (6-DOF) aircraft motion simulation, as might be used for handling quality assessment, body-axis aerodynamic forces and moments are modeled using Taylor series expansions based on force and moment coefficients. Accurate assessment of these force and moment coefficients (magnitudes as well as trends) is critical. Data at high angles of attack, side slip, or high angular rates may be required to model some extreme conditions. Moment coefficients, in particular, are known to be difficult to accurately compute. Since a simulation model is only as good as the data supplied, it is obvious that the input, whether analytical, experimental, or computational, must have high enough fidelity to satisfy the needs of the end user.

An added complication is the dearth of experimental data for benchmarking and validation of S&C predictions. Most existing S&C data consists of integrated forces and moments, with surface pressures in a few cases and flow visualization even less frequently. A critical area of need for CFD-based S&C prediction is that of experimental data with adequate supporting information (e.g., on- and off-body flow physics, model-mount interference information, boundary layer transition detection, and high-fidelity data on tunnel flow characteristics).

With recent advances of CFD technology and the availability of affordable computing power, CFD practitioners using Navier-Stokes solvers have begun to successfully address stability and control problems.¹⁻³ Many experienced analysts

*Senior Research Engineer, Configuration Aerodynamics Branch, Associate Fellow AIAA

[†]Senior Research Scientist, Computational Modeling And Simulation Branch, Member AIAA

[‡]Research Scientist, Computational Modeling And Simulation Branch, Member AIAA

[§]Senior Research Engineer, Vehicle Dynamics Branch, Senior Member AIAA

[¶]Senior Research Engineer, Vehicle Dynamics Branch, Associate Fellow AIAA

This material is declared a work of the U.S. Government and is not subject to copyright protection in the United States.

and designers of aircraft control systems are skeptical for good reasons: fidelity of the database for flight prediction is of critical importance, and the accuracy and productivity of CFD have yet to be validated especially at massively separated flow conditions. To help bridge the gap between CFD practitioners and the S&C community, NASA Langley Research Center hosted the first of several planned COMSAC (*Computational Methods for Stability And Control*) symposia¹ in September 2003. The inaugural symposium sought to encourage discussion of issues that currently limit the use of CFD for S&C applications and to formulate plans for expanded use of CFD in this area.

Subsequent to the symposium, NASA Langley Research Center embarked on a multi-year project to assess state-of-the-art CFD codes for evaluation of both static and dynamic stability derivatives. To support as well as leverage other research work in the Vehicle Systems Program, the focus of the NASA COMSAC effort is a Blended Wing Body (BWB) configuration. The BWB is an advanced-concept vehicle that should offer increased L/D along with reduced takeoff weight and fuel burn over conventional designs.² For aircraft configurations in general, accurate prediction of the longitudinal pitching moment coefficient, C_M , is particularly important, since it would affect configuration design options, the design of the control system, and overall vehicle performance since minimum trim drag is dependent upon accurate prediction of C_M .

This paper describes the initial results for longitudinal static forces and moments obtained from two of the CFD codes under evaluation. These computed results were compared with experimental data for an early version of the Boeing BWB configuration obtained in two NASA Langley wind tunnel facilities using appropriately scaled models for each tunnel. The data include body axis forces and moments, as well as lift and drag. Experimental data were obtained for a number of different slat and elevon configurations. For this initial CFD study, the data used in this paper correspond to configurations with undeflected elevons and leading edge slats.

Description of Wind Tunnel Measurements

Model Descriptions

The wind tunnel data presented in this paper are from a series of tests of a subsonic tri-jet BWB configuration. Two different scale wind tunnel models of an early Boeing blended wing body configuration have been used in tunnel tests: a 2% scale transonic metal model and a 3% scale composite subsonic model. A three-view of the configuration geometry is shown in Figure 1. The moment reference center was 38.67% of the mean aerodynamic chord. The model reference values are listed in Table 1. The models have three pylon-mounted flow-through nacelles located on the upper surface of the aft center-body. The control surfaces consist of 18 elevons, rudder on each winglet and leading edge slats. The two outboard elevons split to serve as both elevons and drag rudders.

The 2%-scale model of the BWB was built for a series of tests in the NASA Langley National Transonic Facility (NTF), including those performed to support CFD code benchmarking for the COMSAC project. For these measurements, all control surfaces and high-lift devices were set at their undeflected positions. Due to the lack of a traditional fuselage and the desire to have no aft-end distortion, the 2% BWB model was fixed to a sting/strut mount attached on the underside of the model as shown in Figure 2. The strut was consisted of a symmetric airfoil to minimize support interference while providing sufficient strength to accommodate the large loads associated with testing in the NTF. The model support system was actuated in pitch by the tunnel control system for angle of attack changes. For the COMSAC investigation, the test was conducted in the NTF tunnel at Mach = 0.2 and three chord Reynolds numbers: $Re_{\bar{c}} = 2.47 \times 10^6$, 3.7×10^6 , and 10×10^6 . The NTF data presented in this paper had post-test correction for tunnel flow angularity, but not been corrected for the influence of the support system.

The 3% low-speed model was designed for both static and dynamic testing and has been used in several tests to date. The data used in this report are from a series of tests in the NASA Langley 14x22-Foot Subsonic Tunnel (hereafter referred to as 14x22-ST) investigating the static and dynamic stability and control characteristics of this configuration over a large angle of attack and sideslip range. For the data reported in this study, the model was mounted in two different configurations, as shown in Figures 3 and 4, intended for static force and moment measurements. Figure 3 shows the relatively large, vertical post mount, attached to the bottom of the model. The post diameter at the model junction was 3 inches. This mounting arrangement was used to measure body axes forces and moments over an angle of attack range from -10° to $+36^\circ$ at dynamic pressures up to $q_\infty = 60 \text{ psf}$, corresponding to a Mach number of $M_\infty = 0.203$ and a Reynolds number based on the mean chord of the model, $Re_{\bar{c}} = 3.76 \times 10^6$.

The second 14x22-ST installation for static measurements had the model mounted through the bottom of the model on a sting/strut with a circular cross section throughout. This support system will be referred to as the small post mount (SP), as shown in Figure 4. The strut diameter of one inch was relatively small as compared to the size of the model and to the diameter of the vertical post mount. This test was used to measure the body axes forces and moments over a large angle of attack and sideslip range.³ The maximum dynamic pressure was $q_\infty = 26 \text{ psf}$ with $M_\infty = 0.134$ and resulted in $Re_{\bar{c}} = 2.47 \times 10^6$.

Wind Tunnel Measurements

Support interference was a major concern for all of these measurements. The influence of the wake and the pressure footprint of the support system on the surface of the model can potentially change the measured forces and moments to a large extent, depending on the angle of attack. While standard tunnel corrections were applied to the measured data, the data presented here were not corrected to account for the influence of the support system. In order to put the data comparisons in perspective, Table 2 shows the 95% confidence level uncertainty for C_N and C_M for four 14x22-ST and NTF tunnel conditions. It should be noted that the reported wind tunnel data are the average values of repeated sampling during the real-time tunnel operation. The actual measurement resolution should be better than the reference uncertainty values cited in Table 2.

Normal force coefficient, C_N , and pitching moment coefficient, C_M , are plotted against angle of attack in Figures 5 and 6, respectively. In Figure 5, both Reynolds number effects and installation effects are noted. A comparison of the 14x22-ST results on the large post (LP) at $M_\infty = 0.203$ and 0.134 , corresponding to $Re_c = 3.7 \times 10^6$ and $Re_c = 2.47 \times 10^6$ shows a slight shift of the normal force curve for angles of attack above about 22° due to the change in the tunnel Mach number, M_∞ and the corresponding Re_c . Likewise, a small but discernible difference in the local slopes of the curves is evident between the blade-mounted NTF data and the post-mounted 14x22-ST data, although it is difficult to distinguish between the large post and small post (SP) results at the scale of the figure.

While Reynolds number effects on C_M are clearly evident for the large post data in Figure 6, more dramatic is the effect of mounting type. The NTF results will be considered as a "baseline" in this figure for comparison purposes since the 2% model was mounted on the streamlined strut described above and illustrated in Figure 2. This faired shape would be expected to produce the relatively smallest wake, and, thus, the smallest pressure footprint on the undersurface of the model behind the strut. On the other hand, the faired strut would produce a flow acceleration on either side of the strut. While the strut position was upstream of the model moment reference center, the reduced pressure in this forward model station could have induced a nose-down pitching moment. In going to the small post mount, a positive (nose-up) shift is noted. Increasing the diameter of the post near the interface with the model to three inches causes a major positive shift relative to the blade mount (LP vs. NTF). The large post clearly produces a significant wake footprint on the lower, aft surface of the model and has a major impact on the pitching moment.

Description of Computational Methods

PAB3D Code Description

PAB3D⁴⁻⁷ is a cell-based, finite volume, structured mesh Navier-Stokes solver. Complex geometries may be accommodated using zonal decomposition with point-matched or flux-conservative patched interfaces. Upwind-biased spatial differencing is used for the convective fluxes; for the results presented here, Roe's flux difference splitting⁸ was employed. The viscous fluxes are centrally differenced using thin-layer approximations in the three generalized coordinate directions. A number of turbulence models are available in the code including the standard $k-\epsilon$ two-equation model, explicit algebraic stress models as formulated by Girimaji⁹ and by Shih, Zhu, and Lumley.¹⁰ For all results presented in this paper, the Girimaji explicit algebraic stress model was used.

To advance the solution in time, PAB3D uses an implicit, backward-Euler time integration. Local time stepping may be used to accelerate convergence to a steady state, or constant time stepping may be used to obtain second-order accurate solutions in time. The latter method was used exclusively for the results presented below. At each time step the linear system is solved using an approximate factorization approach. For time-accurate computations, subiterations are used to reduce the errors arising from linearization and approximate factorization.

FUN3D Code Description

FUN3D¹¹⁻¹³ is a node-based, finite-volume, unstructured mesh Navier-Stokes solver. Within the code, the convective fluxes are computed with one of several available flux-splitting schemes, and for second-order accuracy the values at dual-cell interfaces are reconstructed using gradients at mesh nodes computed via a least-squares technique. For all results presented in this paper, Roe's flux difference splitting was used for the convective fluxes. The full viscous fluxes are discretized using a finite-volume formulation that is equivalent to a Galerkin-type approximation on tetrahedral meshes. For non-tetrahedral meshes, an edge-based formulation is used that retains the complete viscous stresses, without thin-layer approximations. For turbulent flows, both the one-equation model of Spalart and Allmaras¹⁴ (SA) and the two-equation SST model of Menter¹⁵ are available. The SA model may be solved loosely coupled to the mean-flow equations or tightly coupled to the mean-flow equations. Either model is integrated to the wall, without the use of wall functions. For all results presented in this paper, the one equation SA model is employed, solved in a loosely coupled fashion.

FUN3D uses an implicit, backward-Euler time integration algorithm to advance the solution in time. Solutions may be obtained in a second-order, time-accurate manner, using subiterations on the non-linear problem in pseudo time, or with local time stepping to accelerate convergence to a steady state; both techniques were used to obtain the results presented

below. At each time step, the linear system is solved using a point-implicit or line-implicit Gauss-Seidel method; the former was used for these computations.

Computational Model and Grids

The configuration modeled in the computations corresponds to the baseline wind tunnel configuration without slat or elevon deflection. The nacelles are flow through, as in the experiment. Because only longitudinal forces and moments are considered here, half of the configuration is modeled, with symmetry assumed. Significantly, the computational model does not include any mounting hardware or tunnel geometry. Inclusion of these features in the computation is ongoing and will be reported on in the future.

Three different structured grids were used for the PAB3D computations presented below. The first grid, used for the $Re_{\bar{c}} = 2.47 \times 10^6$ computations, consisted of approximately 3.7 million cells. This grid is illustrated in Figure 7, where every other point on the symmetry plane is shown, and is referred to as Grid 1. This grid had wall spacing such that the average y^+ for the $Re_{\bar{c}} = 2.47 \times 10^6$ condition was approximately $y^+ = 0.2$. Grid 2F, used for the $Re_{\bar{c}} = 3.76 \times 10^6$ computations, though similar in layout to Grid 1, was of a different family and contained approximately 5.3 million cells. This grid had wall spacing such that the average y^+ at $Re_{\bar{c}} = 3.76 \times 10^6$ was also approximately $y^+ = 0.2$. In addition, this grid was coarsened by removing every other point in each direction, yielding a mesh of approximately 670,000 cells. This medium grid is illustrated in Figure 8, and is referred to as Grid 2M.

The single unstructured grid used for the FUN3D computations consisted of approximately 2.3 million nodes, with an average y^+ at the $Re_{\bar{c}} = 2.47 \times 10^6$ condition of approximately $y^+ = 0.3$. The unstructured grid on the symmetry plane is shown in Figure 9. Note that when comparing relative grid resolution, the nature of the flow solver must be accounted for; it is appropriate to compare the number of cells in the meshes used for PAB3D (cell based) to the number of nodes in the meshes used for FUN3D (node based). Thus the FUN3D mesh has roughly 60% of the resolution of Grid 1 and roughly 40% of the resolution of Grid 2F. Of course, how the cells and nodes are distributed is very important, but is less easily quantifiable.

CFD Results and Data Comparison

CFD solutions were computed using both codes for two Reynolds numbers: $Re_{\bar{c}} = 2.47 \times 10^6$ and $Re_{\bar{c}} = 3.76 \times 10^6$. The corresponding Mach numbers used for the computations for FUN3D were $M_{\infty} = 0.13$ and $M_{\infty} = 0.20$, each the same as the Mach number at the corresponding experimental test conditions. For the PAB3D computations, the Mach number was $M_{\infty} = 0.23$, a larger than the experimental values to avoid potential convergence degradation when compressible flow solvers are used at low Mach numbers. The total pressure in the computation was adjusted to match the appropriate $R_{\bar{c}}$ for each case.

FUN3D solutions were obtained over a nominal angle of attack range of -10° to $+36^\circ$. However, the exact angle of attack range varied with the Reynolds number. Specifically, the ranges were $\alpha = -5^\circ$ to $\alpha = +35^\circ$ for $Re_{\bar{c}} = 2.47 \times 10^6$, and $\alpha = -8^\circ$ to $\alpha = +36^\circ$ for $Re_{\bar{c}} = 3.76 \times 10^6$. To determine if a steady state had been attained in the computations, the pitching moment coefficient was monitored in addition to density residual. Pitching moment is a more sensitive indicator than either lift or drag, and is the quantity of primary interest from the computations. A steady state was defined as no perceptible variation in pitching moment coefficient over several hundred iterations when plotted on a scale with ranges ± 0.001 about the nominal value. At nearly all angles of attack, steady state solutions were obtained. However, within approximately one degree of $\alpha = 15^\circ$, for all Reynolds numbers, steady state solutions could not be obtained. For these angles of attack, the flow solver was restarted in time-accurate mode, and the unsteady solution was advanced in time for approximately 8-10 cycles of solution oscillation. Time average values of the force and moment coefficients were calculated over the last four cycles, along with the minimum and maximum values. In the figures, the mean values are plotted as symbols, with vertical bars indicating the variation from the mean. It should be noted that all the figures showing FUN3D results have the computed results plotted this way for angles of attack around 15° ; however the variation is really only perceptible on the pitching moment plots, indicating how sensitive an indicator pitching moment is.

The PAB3D solutions were computed over a nominal angle of attack range of -12° to $+36^\circ$. As with the FUN3D cases, the exact range varied with Reynolds number, and with mesh. On Grid 1, the ranges were $\alpha = 0^\circ$ to $\alpha = +15^\circ$ for $Re_{\bar{c}} = 2.47 \times 10^6$. On Grid 2M, the range was $\alpha = -12^\circ$ to $\alpha = +36^\circ$ for $Re_{\bar{c}} = 3.76 \times 10^6$. In addition, a few computations were carried out for $Re_{\bar{c}} = 3.76 \times 10^6$ on Grid 2F over a range of $\alpha = -2^\circ$ to $\alpha = +16^\circ$ to assess the effect of mesh size on the results. All PAB3D solutions were run in a time-accurate manner. On Grid 1, for $Re_{\bar{c}} = 2.47 \times 10^6$, most solutions would not converge to a completely steady state, with small oscillations in force and moment coefficients being observed. The data obtained on Grid 1 were therefore averaged over the last 500 time steps (out of typically 4000 time steps), and these average values are plotted in the figures. Solutions obtained on Grid 2F and Grid 2M for $Re_{\bar{c}} = 3.76 \times 10^6$ did converge to a steady state in all cases, so the final, steady, force and moment values are plotted.

The notation for the experimental data shown in the figures is as follows: 14x22 Exp denotes data taken in the 14x22-ST, with SP used to denote data taken with the model on the small post mount (Figure 4), LP used to denote data taken

with the model on the large post mount (Figure 3); NTF Exp, Run 24X denotes data taken in the NTF with the model on the blade mount (Figure 2), for a particular run number. Because of the proprietary nature of the data, axes showing the force and moment data do not have scales.

Figures 10 and 11 show the comparison between computed and measured normal force coefficients for these two Reynolds numbers. There is little variation among the various tunnel data and the computations. The agreement is slightly better between the computations and the NTF data than between the computations and the 14x22-ST data. The 14x22-ST data, especially for $Re_{\bar{c}} = 2.47 \times 10^6$, show a strong break in slope near $\alpha = 22^\circ$, followed by a continuation of positive slope beyond $\alpha = 25^\circ$. The NTF data were not obtained beyond $\alpha = 16^\circ$, so there is no way to know if a similar trend would be observed in that data set. As for the lower Reynolds number, the computed results do not show this break in slope. Although not evident in the plot, the PAB3D solutions computed for $Re_{\bar{c}} = 3.76 \times 10^6$ on the finer Grid 2F are virtually identical to those computed on the medium Grid 2M over the ranges of angles of attack such that the two PAB3D data sets overlap.

Figures 12 and 13 show the comparison between the axial force coefficients obtained from CFD and experiment. At the higher Reynolds numbers, the axial force coefficient measured in the 14x22-ST increases between $\alpha = 12^\circ$ and $\alpha = 25^\circ$, but decreases with increasing α after that. As with the normal force coefficients, the computed axial force coefficients are in better agreement with the NTF data (limited to $\alpha < 16^\circ$) than the 14x22-ST data. The PAB3D results computed on the finer Grid 2F show slightly better agreement with the NTF data than the Grid 2M results, especially in the range $-2 \leq \alpha \leq 8^\circ$. Apart from the higher angles of attack (beyond $\sim \alpha = 18^\circ$), there is as much variation between the various sets of tunnel data as between the computed results and the tunnel data.

Next, pitching moment coefficient variation with angle of attack is shown in Figures 14 and 15. Pitching moment is far more sensitive to detailed flow phenomenon than either normal or axial force, so it is not surprising to find more variation in C_M between experimental data and computational data, than the data variation in C_A or C_N .

At $Re_{\bar{c}} = 2.47 \times 10^6$, quite a large difference is observed between the 14x22-ST large-post data and the small-post data, particularly for $\alpha < 10^\circ$. The NTF data, though taken over a more limited range, are much closer to the 14x22-ST small-post data. In general, the CFD results are in good agreement with the NTF data.

For $Re_{\bar{c}} = 3.76 \times 10^6$ a similar discrepancy between the 14x22-ST data (large post only) and the NTF data is observed. Again the CFD results lie closer to the NTF data than the 14x22-ST data, with the FUN3D results in generally good agreement with the NTF data. The PAB3D results computed on Grid 2F are nearly identical to those computed on the coarser Grid 2M, although the drop in C_M beyond $\alpha < 14^\circ$ is slightly steeper on the finer mesh.

The pitching moment curves from both the computation and the experiment show a marked variation with angle of attack, suggesting a significant change in flow features over the BWB configuration as the incidence varies. No visualization is available from the tunnel tests, but an indication of the changes that occur can be seen in the CFD solutions. Figures 16 to 18 show the progression in near-surface streamlines along the upper surface as the angle of attack is raised from 5° to 10° to 15° at $Re_{\bar{c}} = 3.76 \times 10^6$. At $\alpha = 5^\circ$, the flow is attached everywhere, with flow predominantly in the axial direction. As the angle of attack is raised to 10° , significant spanwise flow appears on the outboard wing panel. At $\alpha = 15^\circ$, flow separation occurs near the leading edge break, as indicated by the node in the streamline pattern. Virtually the entire outboard wing panel has reversed, spanwise flow at $\alpha = 15^\circ$. Of course, at such a high angle of attack in flight, leading edge slats would be deployed to minimize such undesirable flow.

Concluding Remarks

The results presented here represent a first step toward assessing the usefulness of Navier-Stokes CFD methods for the prediction of parameters relevant to aircraft longitudinal stability. From a static stability point of view, pitching moment coefficient is arguably the most important longitudinal data obtained from either CFD or experiment. This study has brought to light that both CFD solutions and the experimental data have significant variations for any given value of the angle of attack. Hence, not only the CFD solution accuracy should be improved, but the wind tunnel data uncertainties must also be quantified such that the computational methods can be validated to a high level of confidence.

The authors would like to emphasize that the scope of this paper is limited and exploratory in nature, much more remains to be done. The variations between experimental data sets suggest that model mounting systems have a significant effect on the forces and moments for aircraft configurations such as the blended wing body. Comparing the results of the CFD simulations with and without model support may provide a means of correcting the tunnel data to free-flight conditions. Additional areas of consideration are the effects of turbulence models and grid resolutions in the wake region on the accuracy of computational predictions. The inclusion of these considerations in CFD simulations using Navier-Stokes methods is underway.

References

¹Fremaux, C. M., and Hall, R. M. (Compilers): "Computational Methods for Stability and Control". NASA CP-2004-213028 PT1, April 2004.
²Liebeck, R. H.: "Design of the Blended Wing Body Subsonic Transport", Journal of Aircraft, Vol. 41, No. 1, pp 10-25, 2004.

³Vicroy, D. D., Murri, D. G., and Grafton, S. B.: "Low-speed, Large Angle Wind Tunnel Investigation of a Subsonic Blended-Wing-Body Tri-jet Configuration". NASA CDTM-10044, 2004.

⁴Abdol-Hamid, Khaled S., Massey, Steven J., and Elmiligui, Alaa A.: "PAB3D Code Manual". Cooperative development by the Configuration Aerodynamics Branch, NASA Langley Research Center and Analytical Services & Materials, Inc. Hampton, VA.

⁵Uenishi, K. and Abdol-Hamid, K.: "A Three-Dimensional Upwinding Navier-Stokes Code with $k-\epsilon$ Model for Supersonic Flows". AIAA 22nd Fluid and Plasmadynamic Conference, AIAA 91-1669, June 1991.

⁶Abdol-Hamid, K. S.: "Implementation of Algebraic Stress Models in a General 3-D Navier-Stokes Method (PAB3D)". NASA CR-4702, December 1995.

⁷John R. Carlson: "Prediction of Very High Reynolds Number Compressible Skin Friction". 20th AIAA Advanced Measurement and Ground Testing Technology Conference, Albuquerque, New Mexico, AIAA 98-2880, June 15-18, 1998.

⁸Roe, P.; "Approximate Riemann Solvers, Parameter Vectors, and Difference Schemes". *J. Comp. Phys.* Vol. 43, pp 357-372, 1981.

⁹Girimaji, Sharath S.: "Fully-Explicit and Self-Consistent Algebraic Reynolds Stress Model". Institute for Computer Applications in Science and Engineering, 95-82, December 1995.

¹⁰Shih, T.-H., Zhu, J., and Lumley, J. L.: "A New Reynolds Stress Algebraic Model". NASA TM-166644, Institute for Computational Mechanics, 94-8, 1994.

¹¹Anderson, W. K. and Bonhaus, D. L.: "An Implicit Upwind Algorithm for Computing Turbulent Flows on Unstructured Grid". *Computers and Fluids*, Vol. 23, No. 1, pp. 1-21, 1994.

¹²Anderson, W. K., Rausch, R. D., and Bonhaus, D. L.: "Implicit Multigrid Algorithms for Incompressible Turbulent Flows on Unstructured Grids". *J. Comp. Phys.* Vol. 128, 1996, pp. 391-408.

¹³Nielsen, E., Lu, J., Park, M., and Darmofal, D.: "An Implicit, Exact Dual Adjoint Solution Method for Turbulent Flows on Unstructured Grids". *Computers and Fluids*, Vol. 33, No. 9, pp. 1131-1155.

¹⁴Spalart, P. R., and Allmaras, S. R.: "A One-Equation Turbulence Model for Aerodynamic Flows". *La Recherche Aerospatiale* No. 1, 1994, pp. 5-21.

¹⁵Menter, F.: "Improved Two-Equation $k-\omega$ Turbulence Model for Aerodynamic Flows". NASA TM 103975, 1992.

Model scale		2%	3%
Wing area, ft^2	S	5.5627	12.5161
Wing span, ft	b	4.800	7.200
Mean aerodynamic chord, in	\bar{c}	21.364	32.046
Length, in	l	39.564	59.346
Height, in	h	9.660	14.490
Moment ref. center x-coord., in	x_{mrc}	20.927	31.391
Moment ref. center z-coord., in	z_{mrc}	2.683	4.024

Table 1 Model reference values.

Balance	M_∞	$Re_{\bar{c}}$	q_∞, psf	$C_N, 95\% confidence, 2\sigma$	$C_M, 95\% confidence, 2\sigma$
14x22 VST-03	0.203	3.76×10^6	60.	± 0.0076	± 0.00042
14x22 VST-03	0.134	2.47×10^6	26.	± 0.0175	± 0.00096
NTF-113B	0.20	3.7×10^6	93.5	± 0.0063	± 0.00039
NTF-113B	0.20	2.47×10^6	62.4	± 0.0095	± 0.00058

Table 2 Balance accuracy at selected tunnel conditions.

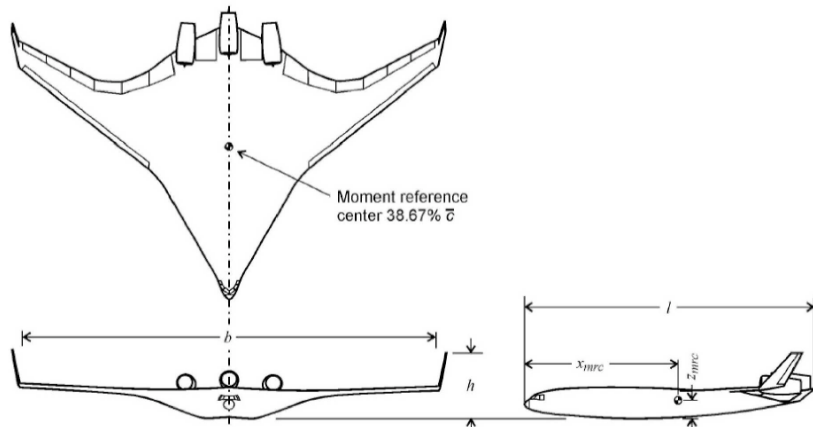


Fig. 1 Three-view of Boeing blended wing body BWB-450L configuration.



Fig. 2 2% scale BWB model on a blade-mounted installation in the National Transonic Facility (NTF).

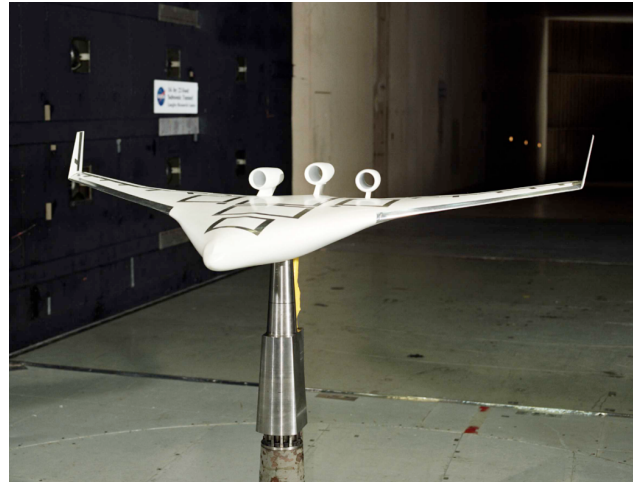


Fig. 3 3% scale BWB model mounted on the large-post model support in the 14 x 22 Foot Wind Tunnel.

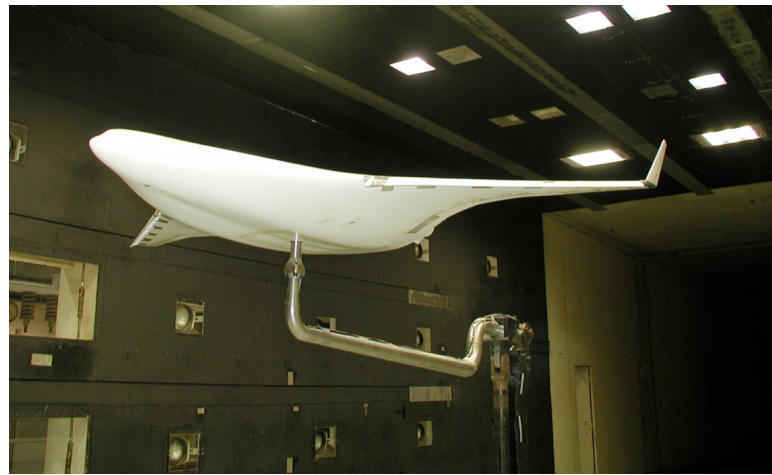


Fig. 4 3% scale BWB model mounted on the small-post model support in the 14 x 22 Foot Wind Tunnel.

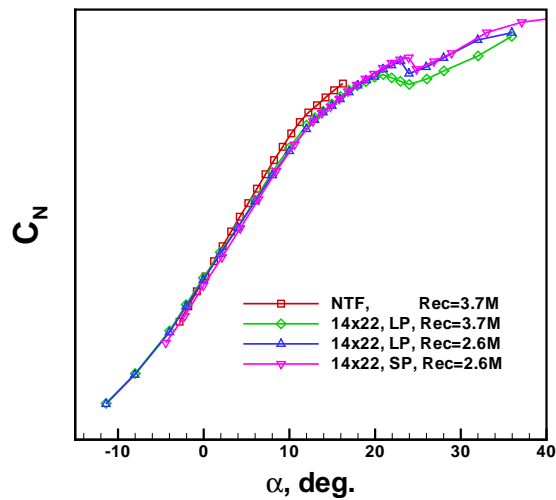


Fig. 5 Measured normal force coefficient comparison at $Re_{\bar{c}} = 2.6 \times 10^6$ and $Re_{\bar{c}} = 3.7 \times 10^6$ with different mounting arrangements.

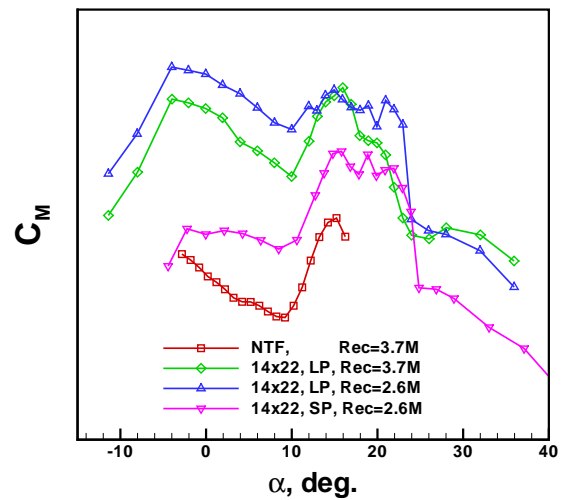


Fig. 6 Measured pitching moment coefficient comparison at $Re_{\bar{c}} = 2.6 \times 10^6$ and $Re_{\bar{c}} = 3.7 \times 10^6$ with different mounting arrangements.

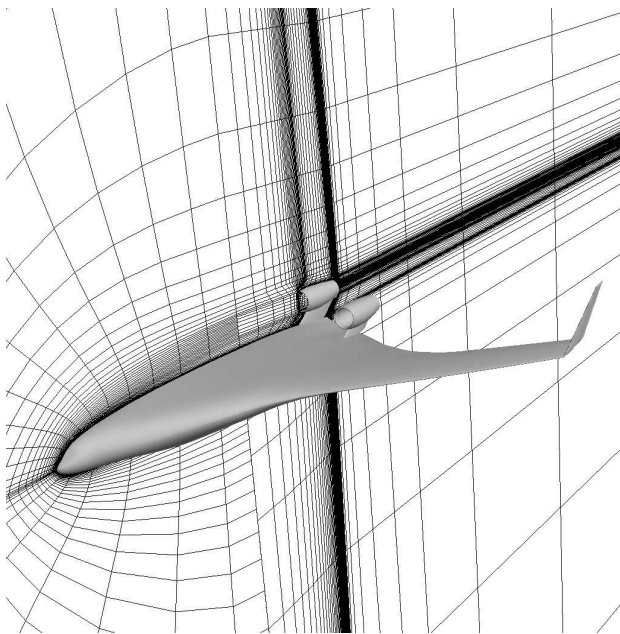


Fig. 7 Structured grid used in PAB3D computations for $Re_{\tilde{c}} = 2.47 \times 10^6$ ("Grid 1"); every other point shown.

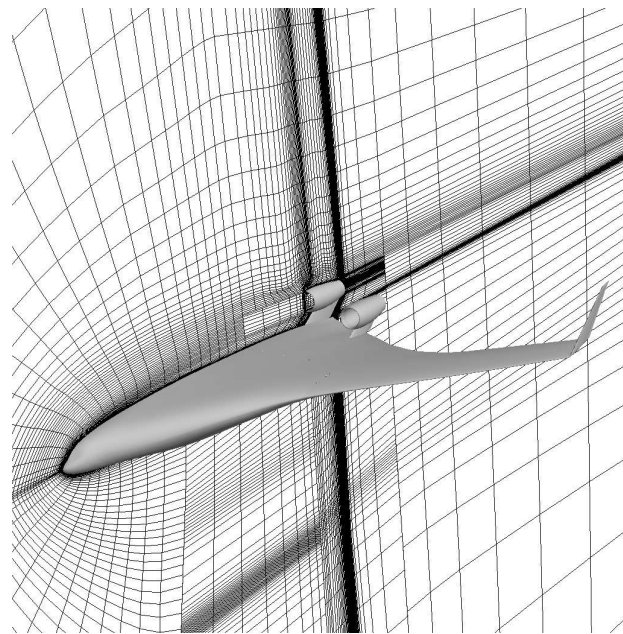


Fig. 8 Structured grid used in PAB3D computations for $Re_{\tilde{c}} = 3.76 \times 10^6$ ("Grid 2F"); every other point shown, corresponding to the medium mesh ("Grid 2M").

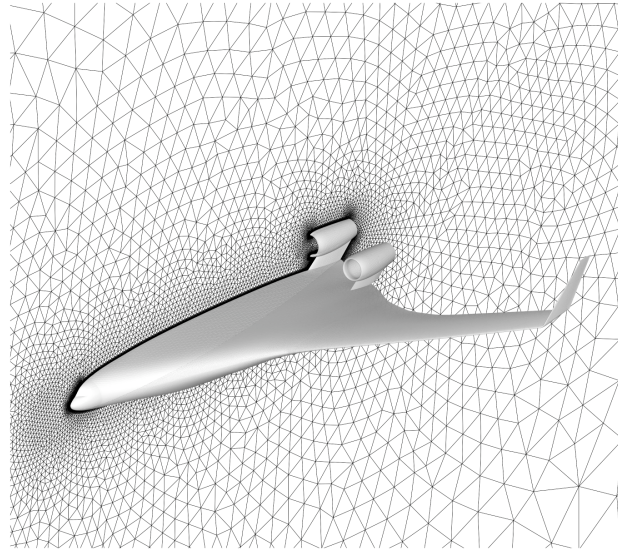


Fig. 9 Unstructured grid used for FUN3D computations.

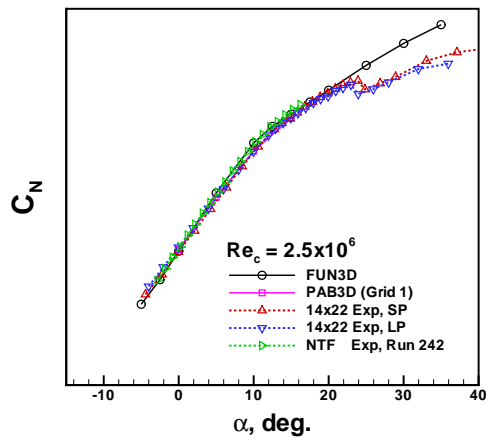


Fig. 10 Normal force coefficient comparisons between CFD solutions and wind tunnel data at $Re_c = 2.47 \times 10^6$.

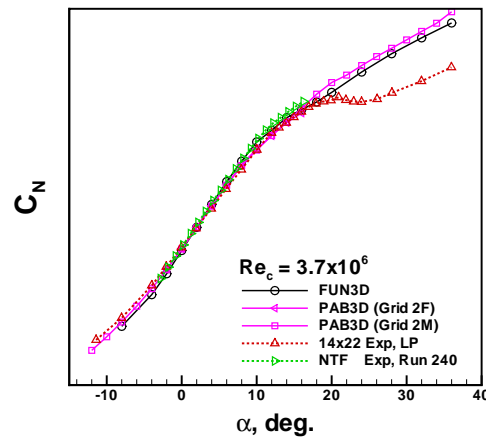


Fig. 11 Normal force coefficient comparisons between CFD solutions and wind tunnel data at $Re_c = 3.76 \times 10^6$.

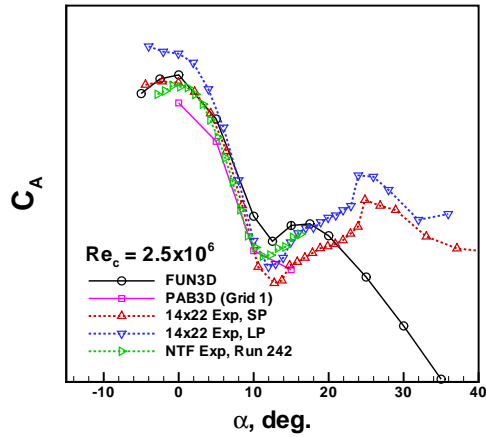


Fig. 12 Axial force coefficient comparisons between CFD solutions and wind tunnel data at $Re_c = 2.47 \times 10^6$.

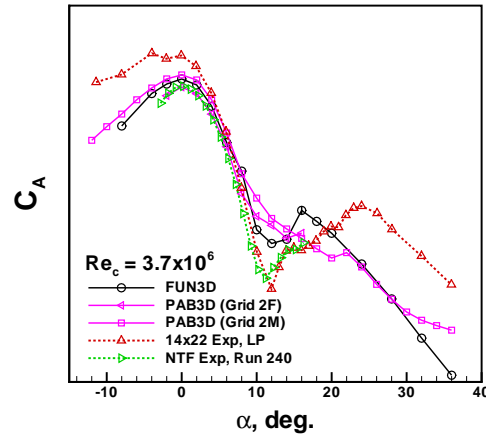


Fig. 13 Axial force coefficient comparisons between CFD solutions and wind tunnel data at $Re_c = 3.76 \times 10^6$.

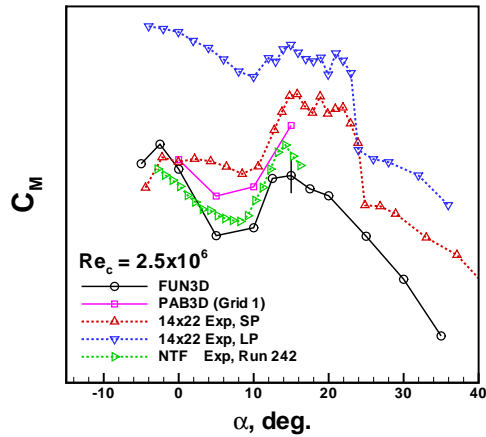


Fig. 14 Pitching moment coefficient comparisons between CFD solutions and wind tunnel data at $Re_c = 2.47 \times 10^6$.

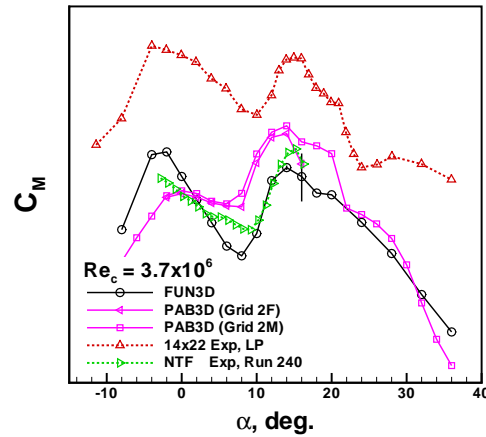


Fig. 15 Pitching moment coefficient comparisons between CFD solutions and wind tunnel data at $Re_c = 3.76 \times 10^6$.

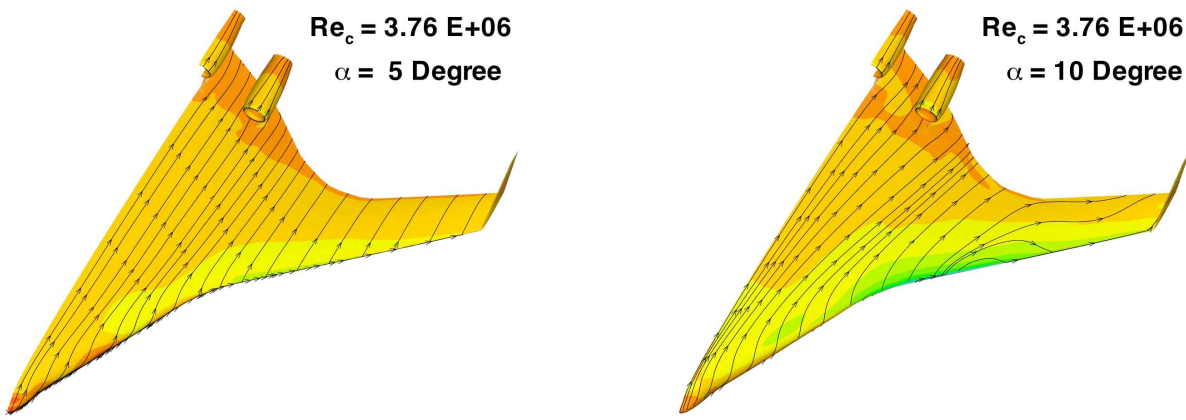


Fig. 16 Surface streamline traces at $\alpha = 5^\circ$, $Re_c = 3.76 \times 10^6$.

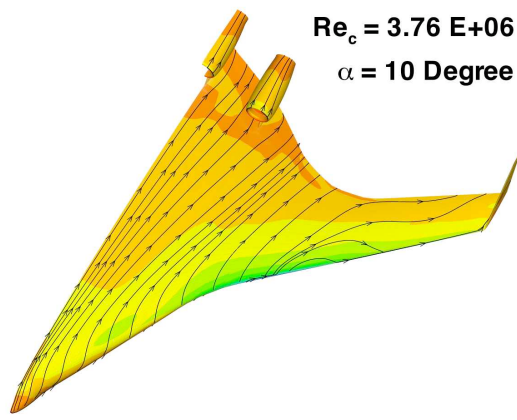


Fig. 17 Surface streamline traces at $\alpha = 10^\circ$, $Re_c = 3.76 \times 10^6$.

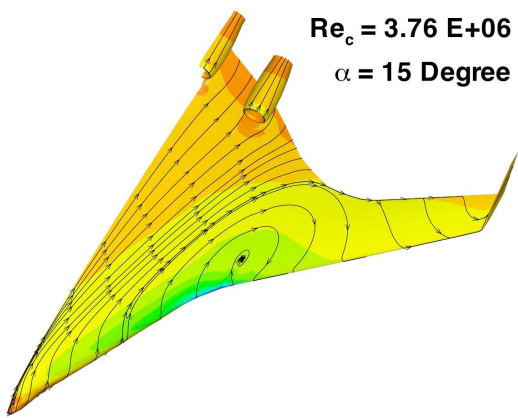


Fig. 18 Surface streamline traces at $\alpha = 15^\circ$, $Re_c = 3.76 \times 10^6$.